Transport in Porous Media (2021) 139:203–221
https://doi.org/10.1007/s11242-021-01654-7

Pore-Scale Numerical Investigation of Evolving Porosity and Permeability Driven by Biofilm Growth

Heewon Jung[1,2] · **Christof Meile**[1]

Received: 4 September 2020 / Accepted: 9 July 2021 / Published online: 27 July 2021

Abstract

Microorganisms in natural porous media can form biofilms that alter the pore structure and medium permeability. This affects fluid flow and solute transport, with bioclogging shaping the efficiency of, for example, bioremediation and hydrocarbon recovery. Here, we investigate the effect of biofilm growth on fluid flow across a wide range of flow and reaction conditions using pore-scale numerical simulations in idealized porous media. The simulation results show preferential biofilm growth and pore closure near the source of a growth-limiting substrate. This spatially heterogeneous biofilm growth at the pore scale affects the evolution of porosity and permeability. When approaching pore closure, permeability can change significantly without large changes in porosity, differentiating this setting from the empirical porosity–permeability relationships such as the Kozeny–Carman (KC) equation commonly used at the bulk scale. We find for impermeable biofilms that spatially non-uniform biofilm growths depend strongly on Péclet (*Pe*) and diffusive Damköhler numbers (*Da*) governing heterogeneous substrate distribution. We also demonstrate that *Pe* and *Da* can describe the evolution of porosity and permeability of porous media with various pore geometries, including pore throat size and tortuosity. Finally, the simulations with porous and permeable biofilms reveal significantly different evolution of porosity and permeability compared to non-porous and impermeable biofilms, highlighting the importance of micro-scale biofilm characteristics for macro-scale hydrological properties of porous media.

Keywords Bioclogging · Permeability evolution · Biofilm porosity · Biofilm permeability

Abbreviations

f	Distribution function of water
g	Distribution function of substrate concentrations
$\boldsymbol{r}$	Position vector
Δt	Time step
Ω	Collision operator
$\boldsymbol{c}$	Lattice velocity
$\boldsymbol{u}$	Macroscopic velocity

✉ Heewon Jung
hjung@cnu.ac.kr

[1] Department of Marine Sciences, University of Georgia, Athens, GA, USA

[2] Department of Geological Sciences, Chungnam National University, Daejeon, South Korea

c_s	Speed of sound
ρ	Macroscopic density
ω	Lattice weights
τ_f	Relaxation time for the distribution function f
τ_g	Relaxation time for the distribution function g
ν_{f}	Kinematic viscosity of water
ν_{bf}	Kinematic viscosity of water in the biofilm
L_x	Domain length in x-direction
L_y	Domain length in y-direction
ΔP	Pressure differences
D	Diffusivity
X	Viscosity ratio for biofilm permeability
ϕ	Porosity
ϕ_0	Initial porosity
ϕ_c	Critical porosity
ϕ_{BPs}	Biofilm porosity
ϕ_{thrd}	Threshold porosity
ϕ_R	Porosity at the maximum reaction rate
κ	Permeability
U	Average flow velocity
l	Characteristic length
l_ϕ	Pore throat size
V_T	Total volume
V_P	Pore volume
V_{BF}	Biofilm volume
k	Rate constant
B	Biomass density
K_M	Half-saturation constant
C	Substrate concentration
R_B	Biomass growth rate
R_C	Solute consumption rate
B_{max}	Maximum biomass density
Ma	Mach number
Pe	Péclet number
Da	Diffusive Damköhler number
λ, β	Free parameters for the Kozeny–Carman equation
F	Scaling factor for initial porosities

Simulations

BF	Non-porous impermeable biofilm
PB	Non-porous permeable biofilm
BP	Porous permeable biofilm
GM	Non-porous impermeable biofilm with varying geometries
NBF*	Non-porous impermeable biofilm with uniform thicknesses
HPB*	Non-porous highly permeable biofilm with uniform thicknesses
LPB*	Non-porous less permeable biofilm with uniform thicknesses
NBP*	Porous impermeable biofilm with uniform thicknesses

HBP* Highly porous and highly permeable biofilm with uniform thicknesses
LBP* Less porous and less permeable biofilm with uniform thicknesses

1 Introduction

Microorganisms often form biofilms in natural porous media and drive biogeochemical processes of many elements (Stoodley et al. 2002). Such formation of biofilms is critical in many engineering applications such as wastewater treatment (Miranda et al. 2017), biocatalysis for chemical syntheses (Halan et al. 2012), and enhanced oil recovery (Han et al. 2014; Hosseininoosheri et al. 2016). With sufficient supply of nutrients, biofilm growth can lead to pore clogging that causes significant changes in flow and solute or colloidal transport (Abdel Aal et al. 2010; Baveye et al. 1998; Cunningham et al. 1991). Bioclogging can result in damage to mechanical systems and severe loss of efficiency in bioremediation (Ellis et al. 2000; Lendvay et al. 2003), but it can also be utilized in well-curated engineering strategies. For example, selective bioclogging of preferential flow paths has been used to recover residual petroleum in low permeability regions in enhanced oil recovery (Lazar et al. 2007), and biofilms degrading contaminants can also restrict the subsurface contamination plume from spreading (Kao et al. 2001; Komlos et al. 2004). Therefore, it is essential to properly estimate the impact of biofilms on flow and transport characteristics of porous media.

Microbial growth in porous media is affected by hydrological features, such as pore geometry and interstitial flow velocity, requiring pore-scale investigation for precise evaluation of bioclogging (Carrel et al. 2018; Heße et al. 2009; Stolpovsky et al. 2012). However, the scales of common engineering practices span meters to kilometers. For practical applications, therefore, it is necessary to represent pore-scale processes with a small number of macroscopic parameters (Battiato et al. 2009; Quintard and Whitaker 1994; Wood 2009). Two essential hydrologic parameters altered by biofilm growth are porosity and permeability, which have been related to each other through empirical models, including the Kozeny–Carman equation and power law relations (Hommel et al. 2018; Luquot and Gouze 2009; Xie et al. 2015). These models account for the morphological complexity of natural porous media using measurable parameters, such as tortuosity, grain shapes, and specific surface area (Schulz et al. 2019). However, these approximations can deviate substantially from actual permeabilities in heterogeneous porous media (Mostaghimi et al. 2013; Vandevivere 1995). Furthermore, these semi-empirical porosity–permeability models commonly do not account for the feedback of reactions on the flow and transport characteristics of porous media (Kang et al. 2003).

Numerical studies have revealed that different porosity and permeability relationships arise as a result of mineral dissolution and precipitation reactions under different flow velocity (Péclet Number, *Pe*) and reaction rate (diffusive Damköhler number, *Da*) conditions (Golfier et al. 2002; Kang et al. 2003; Soulaine et al. 2017). The evolution of porosity and permeability induced by biofilm growth is expected to be even more pronounced because exponentially increasing biomass might accelerate microbially mediated reactions over time, while mineral reactions are limited to gradually evolving water–rock interfaces (Ezeuko et al. 2011; Peszynska et al. 2016; Pintelon et al. 2009). However, unlike for mineral reactions, the porosity and permeability evolution induced by biofilm growth under various *Pe* and *Da* conditions remains largely unexplored.

Another important feature shaping bioclogging is the porosity and permeability of the biofilm itself. Many pore-scale biofilm models have assumed that biofilms are non-porous and impermeable while mass exchange occurs only through diffusion (e.g., Heße et al. 2009; Jung and Meile 2019; Tang et al. 2013). However, biofilms often exhibit high porosities (Cunningham et al. 1991; Zhang and Bishop 1994) and can contain micro-channels that facilitate solute transport through biofilms (Rooney et al. 2020; Wilking et al. 2013). This can enhance nutrient delivery to microbes in biofilms and determine biofilm growth dynamics and evolution of system porosity and permeability (Pintelon et al. 2012; Thullner and Baveye 2008).

In this study, we investigate the evolution of porosity and permeability using a pore-scale reactive transport modeling approach to provide systematic and comprehensive analysis on the effect of various pore-scale features on evolving porous media induced by biofilm growth. To investigate the effect of *Pe* and *Da* on the evolution of porosity and permeability, a series of simulations across an environmentally relevant range of *Pe* and *Da* were carried out where non-porous impermeable biofilms grow in an idealized porous medium. Here, the widely used Kozeny–Carman (KC) equation (e.g.,. Xie et al. 2015) was chosen as the reference frame to discuss the porosity–permeability evolution observed in our pore-scale simulation results. We also explore the effect of variations in pore geometries, including pore throat size and tortuosity. Finally, we relax the impermeable biofilm assumption and investigate the effect of biofilm porosity and permeability on the evolution of porous media.

2 Methods

A two-dimensional pore-scale reactive transport model was developed using the open source Lattice Boltzmann (LB) code *palabos* (Latt et al. 2021), leveraging the LB model implementations presented in Jung and Meile (2019; 2020). Fluid flow was simulated by solving the discretized Boltzmann equation:

$$f_i\left(\mathbf{r}+\boldsymbol{c}_i\Delta t, t+\Delta t\right) = f_i(\mathbf{r},t) + \Omega_i^{BGK}(\mathbf{r},t) \tag{1}$$

where f_i(**r**,t) is the ith discrete set of particles streamed from a position **r** to a new position $\mathbf{r}+\boldsymbol{c}_i\Delta t$ after a time step Δt with lattice velocities $\boldsymbol{c}$, using a D2Q9 lattice. The collision operator (BGK; Bhatnagar et al. 1954) is given by

$$\Omega_i^{BGK}(\mathbf{r},t) = \frac{\Delta t}{\tau}\left[\omega_i\rho + \omega_i\rho_0\left(\frac{\mathbf{u}\cdot\boldsymbol{c}_i}{c_s^2} + \frac{\left(\mathbf{u}\cdot\boldsymbol{c}_i\right)^2}{2c_s^4} - \frac{\mathbf{u}\cdot\mathbf{u}}{2c_s^2}\right) - f_i(\mathbf{r},t)\right] \tag{2}$$

where ω_i are the lattice weights for a D2Q9 lattice, τ is the relaxation time, ρ is the macroscopic density ($\rho = \Sigma f_i$), ρ_0 is the rest state constant, **u** is the macroscopic velocity calculated from the momentum ($\rho\mathbf{u} = \Sigma\, \boldsymbol{c}_i f_i$), and c_s is a lattice-dependent constant.

Solute and biomass transport were simulated with a distribution function, g

$$g_i\left(\mathbf{r}+\boldsymbol{c}_i\Delta t, t+\Delta t\right) = g_i(\mathbf{r},t) + \Omega_i^{BGK}(\mathbf{r},t) + \Omega_i^{RXN}(\mathbf{r},t) \tag{3}$$

with a BGK operator (Ω_i^{BGK}; Eq. 2) and a reaction term (Ω_i^{RXN}; Eq. 4). The D2Q5 lattice was chosen for numerical efficiency (Krüger et al. 2017), where ω_i are the lattice weights

for a D2Q5 lattice with lattice velocities $\boldsymbol{c}_i$. The solute consumption reaction rate (R_C) was represented by Michaelis–Menten kinetics so that:

$$\Omega_i^{RXN}(\mathbf{r},t) = \Delta t \omega_i R_C = -\Delta t \omega_i k B \left(\frac{C}{K_M + C} \right) \tag{4}$$

where k is the rate constant, B is biomass density, K_M is the half-saturation constant set to 0.16 mM (estimated for acetate; MacQuarrie and Sudicky 2001), and C is the solute concentration. The Chapman–Enskog analysis of Eqs. 1 and 3 yields the Navier–Stokes and advection–diffusion–reaction equations with a kinematic viscosity $\nu_f = c_s^2\left(\tau_f - \frac{\Delta t}{2}\right)$ and diffusivity $D = c_s^2\left(\tau_g - \frac{\Delta t}{2}\right)$ with the relaxation time for flow solver (τ_f) and transport solver (τ_g) , respectively.

Biofilm growth was simulated using a cellular automaton approach (Picioreanu et al. 1998; Tang et al. 2013). The rate of biomass growth (R_B) was calculated for each grid cell, assuming a net growth efficiency of 0.1 ($R_B = 0.1R_C$) while ignoring sinks of microbial biomass (e.g., detachment, which would potentially spread cells and biofilm growth downstream; or cell death, counteracting rapid growth). After updating the biomass density of every grid cells, any biomass that exceeded the maximum biomass density ($B > B_{max}$, where B_{max} is the maximum biomass density allowed for a grid cell) was redistributed as follows: First, pore and biomass grid cells adjacent to the cell with excess biomass were identified and one cell among them was randomly selected. All the excess biomass was moved to the selected grid cell if the biomass of the selected cell did not exceed B_{max} after redistribution. If the selected cell was not able to hold all the excess biomass, the remaining excess biomass was placed to another randomly selected grid cell. If all the neighboring cells had biomass densities larger than or equal to B_{max}, the distances of the neighboring cells from the solid interface were evaluated and the excess biomass was placed in a grid cell that was further away or had the equal distance from the solid among the neighboring grid cells. This biomass redistribution was repeated until all the excess biomass was redistributed (Benioug et al. 2017). A theoretical upper limit of excess biomass travel distance for impermeable biofilm simulations corresponds to the width of a pore throat, approximately 25 grid cells, as the simulations were terminated at the point of complete pore closure. Pore cells were designated as biomass cells, in which solute transport occurred only through diffusive transport, once the biomass reached a threshold density ($B \geq 0.5B_{\max}$; Benioug et al. 2017; Huber et al. 2014). Biomass density and substrate transport were updated every time step, while the flow field was updated every 10 time steps. This decoupling significantly reduced computing time and has been employed in investigating biofilm-induced evolution of pore geometry (Thullner and Baveye 2008).

Numerical simulations were carried out in 2D domains with simplified pore geometries consisting of circular solids (Fig. 1 and Table 1). The domain was discretized into 1100×100 elements including two reservoirs of 50×100 at the left and right side of the domain for numerical stability (Fig. 1). Biofilms were distributed with an initial density of $0.1B_{max}$ at each pore grid cell along the solid–fluid boundary grid cells, and a growth-limiting nutrient was injected at the left domain boundary. This highly simplified and idealized pore geometry helps clarify the governing processes and hence, has been used to, for example, validate theoretical upscaling schemes (Davarzani et al. 2010), and study the evolution of the porosity–permeability relationship during calcite dissolution reactions (Soulaine et al. 2017).

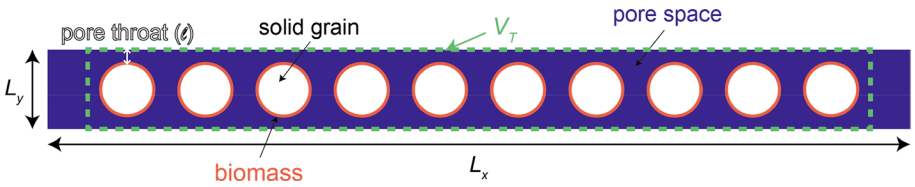

Fig. 1 Schematic illustration of a porous medium used for numerical simulations. It consists of 10 circular solid grains (white). Biomass (red) was initially distributed along the surface of solid grains. The dashed green line indicates the volume for which porosity and permeability are calculated (V_T)

Table 1 Simulation conditions used for dynamic biofilm growth, including impermeable biofilms (BFs; $X=\nu_f/\nu_{bf}=0$), permeable non-porous biofilms (PBs; $X>0$), impermeable and permeable porous biofilms (BPs; $\phi_{BP}>0$), and varying geometries (GMs) of impermeable biofilms

Case name	X	ϕ_{BP}	Pe	Da	Geometry
BF1 - BF100	0	0	0.17 - 1.70	0.18 - 1.81	
PB1	0.33	0	0.85	0.18	
PB2	0.03				
PB3	0.33		0.17	0.90	
PB4	0.03				$\phi_0 = 0.6564$, $l_1 = 0.17L_y$
PB5	0.33		0.85	0.90	
PB6	0.03				
BP1	0.33	0.9	0.85	0.09	
BP2	0.03	0.63		0.33	
BP3	0	0.56		0.40	
BP4	0	0.56		0.90	
GM1	0	0	0.85	0.90	$\phi_0 = 0.6564$, $l_1 = 0.17L_y$ GM1 GM2
GM2					
GM3			1.20	1.80	$\phi_0 = 0.7812$, $l_2 = 0.24L_y$
GM4			0.50	0.31	$\phi_0 = 0.4860$, $l_3 = 0.1L_y$
GM5			1.24	1.91	$\phi_0 = 0.6568$, $l_4 = 0.247L_y$ GM5 GM6
GM6					

Where the grain arrangement at the left and right boundaries differs (GM1&2 and GM5&GM6), arrows indicate flow directions. The index for case BF represents [(*Pe* entry $-1)\times 10+Da$ entry] in the sets of $Pe\in\{0.17, 0.34, 0.51, 0.68, 0.85, 1.02, 1.19, 1.36, 1.53, 1.70\}$ and $Da\in\{0.18, 0.36, 0.54, 0.72, 0.90, 1.08, 1.26, 1.45, 1.63, 1.81\}$

Fluid flow in the porous medium was induced by imposing a fixed pressure gradient ($\Delta P/L$) between inlet and outlet boundaries, and no-slip boundaries were imposed at the top and bottom of the domain. The Mach number was kept low ($\mathrm{Ma}=\mathbf{u}/c_s \ll 1$) to ensure incompressible flow conditions. No-slip boundary conditions were imposed for the flow solver (Eq. 1) at the biomass/fluid interfaces and solid/fluid interfaces for impermeable and permeable biofilms, respectively, using the bounce-back algorithm (Ginzbourg and Adler 1994). Fluid flows in permeable biofilm grid cells were approximated by increasing the kinematic viscosity in the biofilm (ν_{bf}) with $\nu_{bf}=\nu_f/X$, where X are 0.333 and 0.033 for high and low biofilm permeabilities, respectively, adopting values used by Pintelon et al. (2012). For solute transport, the initial substrate concentration was set to 1 mM, which was also set at the inlet boundary at the left of the domain (Fig. 1). A no-gradient boundary condition was applied at the outlet, and no-slip

boundaries were imposed at the top and bottom boundaries. Inside the domain, a no-slip boundary condition was applied at the solid/fluid interfaces, allowing for diffusive substrate transport through biomass grid cells with a reduced diffusivity of $0.8D$ (Tang et al. 2013). The simulations for impermeable and permeable biofilm were terminated at the point of percolation limit (Sects. 3.1–3.2) and at an arbitrary time point after the pore throat nearest to the inlet is completely filled with biomass (Sects. 3.3–3.4), respectively.

The porosity–permeability relationship in different flow and reaction conditions was explored through 100 simulations with impermeable biofilms (BF1–BF100), covering a range of Péclet ($Pe = 0.17–1.70$) and diffusive Damköhler numbers ($Da = 0.18–1.81$; see Table 1) defined as:

$$Pe = \frac{Ul}{D} \tag{5}$$

$$Da = \frac{kB_{max}l^2}{K_M D} \tag{6}$$

where U is the average flow velocity at $t = 0$, and l is the characteristic length scale set to the pore throat size ($l_{1\text{-}4}$; see column "Geometry" in Table 1). When modifying Da, k was changed while fixing B_{max} to maintain the same biofilm expansion characteristics. The minimum Da value of 0.18 was determined with $k = 100$ day^{-1} (MacQuarrie and Sudichky 2001), $B_{max} = 900$ mol m^{-3} (Rittmann and McCarty 2001), and $l_1 = 170$ µm. Note that Pe and Da are computed for the initial flow and reaction conditions. For six permeable biofilm simulations (PB1–PB6), three different combinations of Pe and Da were chosen for each of the viscosity ratios X of 0.33 and 0.03. For porous biofilms (BP1–BP4), three biofilm porosities $\phi_{\mathrm{BPs}} = 0.56$, 0.63, and 0.9 were assigned to biofilm grid cells (covering the range reported in Zhang and Bishop 1994), with viscosity ratios $X = 0$, 0.03 and 0.33, respectively. B_{max} was adjusted to reflect the biofilm porosity, i.e., $B_{max,\mathrm{BPs}} = (1-\phi_{BPs}) \times B_{max,\mathrm{BF45}}$, while assuming no contribution of biofilm porosity to total porosity ($\phi = V_p / V_T$; where V_p = pore volume, V_T = total volume). For BP1-3, the same Pe and $kl^2/K_M D$ ($= Da/B_{max}$) conditions as BF45 were used. For BP4, k was increased to match Da of BF45 because the adjustment of B_{max} alters Da (Table 1). The effects of pore scale geometric factors, including tortuosity and pore throat size (l), on permeability were investigated by systematically varying pore geometries (GM1–GM6, Table 1) while maintaining U/D ($= Pe/l$) and $kB_{max}/K_m D$ ($= Da/l^2$) of the reference case, BF45 ($Pe = 0.85$ and $Da = 0.90$; Table 1).

In addition to a total of 116 dynamic biofilm growth simulations, 50 flow simulations were carried out to construct the porosity–permeability relationships in the presence of uniformly distributed biofilms of constant thickness (Table 2; 16 impermeable biofilms (NBFs*), 17 non-porous permeable biofilms for each $X = 0.333$ (HPBs*) and 0.033 (LPBs*)). An additional 50 porous uniform biofilm cases (NBPs*, LBPs*, HBPs*) were estimated by calculating macroscopic porosities with the assigned biofilm porosity ϕ_{BP} of 0.56, 0.63, and 0.9 while using the same permeabilities from the non-porous permeable biofilm simulations (NPBs*, LPBs*, HPBs*).

Macroscopic porosity (ϕ) and permeability ($\kappa = -\nu_f \rho U_x L/\Delta P$; where κ = permeability, U_x = the average x-directional flow velocity, ΔP = pressure difference) of dynamic simulations were calculated periodically. The simulation results were compared to the Kozeny–Carman equation (Schulz et al. 2019) as a general frame of reference for our pore-scale simulation results:

Table 2 Static biofilm simulations with pre-defined uniform biofilm thicknesses for non-porous impermeable biofilms (NBFs*), non-porous highly permeable biofilms (HPBs*), non-porous less permeable biofilms (LPBs*), porous impermeable biofilms (NBPs*), highly porous permeable biofilms (HBPs*), and less porous permeable biofilms (LBPs*)

Case name	ϕ_{BPs}	X	Geometry
NBF1*–NBF16*	0	0	$\phi_0 = 0.6564$, $l_1 = 0.17L_y$
HPB1*–HPB17*	0	0.33	
LPB1*–LPB17*	0	0.03	
NBP1*–NBP16*	0.56	0	
HBP1*–HBP17*	0.9	0.33	
LBP1*–HBP17*	0.63	0.03	

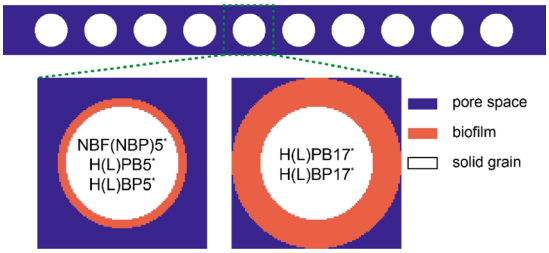

Asterisk indicates static (no growth) biofilms; the number of each case name (s) reflects the biofilm thickness $s/100 \times L_y$ (e.g., biofilm thickness of NBF5* = HPB5* = LPB5* = NBP5* = HBP5* = LBP5* = $0.05L_y$). Examples of biofilm distribution with two different biofilm thicknesses ($0.05L_y$ and $0.17L_y$) are shown with the domain geometry used for static simulations

$$\left(\frac{\kappa}{\kappa_0}\right)_{KC} = \lambda \frac{(\phi - \phi_c)^3}{(1-\phi)^\beta} \tag{7}$$

where ϕ_c is the critical porosity ($\phi_c = 1-\pi/4$), at which porous media loses hydrologic connectivity for simulations with non-porous impermeable biofilm (NBFs* and BFs), and two free parameters ($\lambda = 10.15$, $\beta = 0.12$) were estimated by fitting the data of NBFs* (Table 2 and Fig. 2a).

3 Results and Discussion

3.1 Permeability Reduction Under The Growth of Non-Porous Impermeable Biofilms

The simulation results illustrate that the early stage evolution of ϕ and κ induced by biofilm growth is well represented by the KC equation (Fig. 2a). However, as biofilms grow over time (i.e., decreasing ϕ), the simulated permeabilities drop below the KC curve (symbols representing simulations deviate from the red KC fit; Fig. 2a). Investigating an early time point of BF21 (P1; Fig. 2a) reveals that the biofilm is distributed uniformly because substrate removal is limited at low biomass density (B), and thus, the substrate concentrations, consumption, and growth rates are rather homogeneous throughout the domain (Fig. 2b). At this stage, the substrate consumption rate ($<R_c> = \int R_c dV_T / \phi_0 V_T$) increases with biofilm growth because the increase in cell numbers outweighs the reduction in permeability and solute influx (Fig. 2c). At later times (e.g., P2), however, the decrease in substrate influx becomes a limiting factor, lowering $<R_c>$ (i.e., at porosities lower than the porosity at which $<R>$ is maximal; Fig. 2c). Reduced interstitial velocity also increases the residence time of the injected solute, allowing upstream biofilms more time to consume

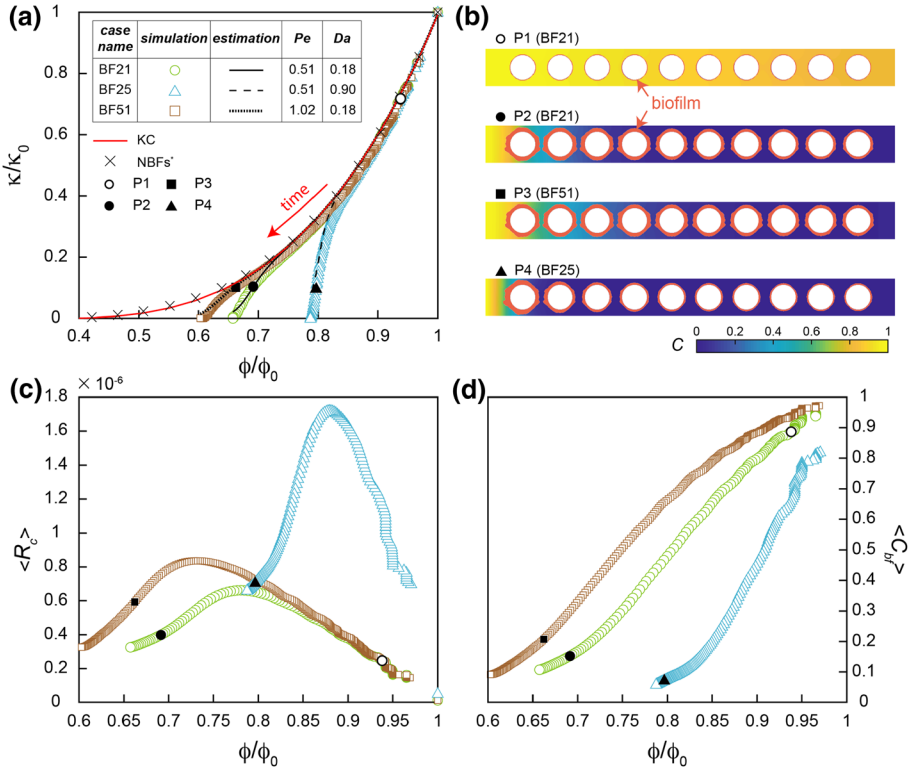

Fig. 2 (**a**) The porosity (ϕ) and permeability (κ) relations of three simulations with different *Pe* and *Da* (BF21, BF25, BF51). The Kozeny–Carman (KC) curve (Eq. 7; red line) is plotted with NBFs* (×markers) used for estimating λ and β of Eq. 7. Black lines are the estimated ϕ-κ curves from the empirical equations (Equations S1 and S2). One early time point (P1) and three late time points (P2—P4) are selected to show (**b**) spatial biofilm and substrate distribution, (**c**) volume-averaged substrate consumption rate ($<R_c>$) and (**d**) volume-averaged concentration distribution within biofilm grid cells ($<C_{bf}>$)

the injected substrate before the solute is transported downstream. As a result, biofilms near the inlet rapidly consume the injected substrate, providing only a small fraction of the substrate to downstream regions. For example, the substrate concentration near the inlet (x-grid point $nx=70$ out of 1100, y-grid point $ny=35$ out of 100) and downstream ($nx=370$, $ny=35$) locations decreases from 0.99 to 0.92 at a time point P1 to 0.83 and 0.06 at P2. This rapid substrate consumption near the inlet results in preferential upstream biofilm growth and limited growth downstream (e.g., R_B ($nx=70$, $ny=35$) $=3.07\times R_B$ ($nx=370$, $ny=35$) at P2).

The permeability in the simplified regular porous media of this study is determined primarily by the pore throat size at the left-most solid grain where biofilms grow preferentially, ultimately disrupting hydrologic connectivity even if there was little biofilm growth further downstream. Because the porosity calculation includes biofilms throughout the entire domain, the preferential biofilm growth results in complete pore clogging at a higher porosity than if biofilm growth was uniform within the model domain. This observation suggests that the scales of representative elementary volumes (REVs) for permeability and porosity evolve differently as a result of spatially heterogeneous biofilm growth. Therefore,

the slopes of ϕ-κ curves increase rapidly with preferential biofilms growth near the inlet and no longer be captured by the KC equation postulating the same REV scale for both porosity and permeability (Schulz et al. 2019). These simulation results correspond to the observation that KC overestimates permeability because of disproportional closure of pore throats (Doyen 1988).

Comparing ϕ-κ curves from simulations that differ only in flow (i.e., *Pe*; BF21 vs. BF51) or reaction conditions (i.e., *Da*; BF21 vs. BF25) shows that low *Pe* and high *Da* lead to highly non-uniform biofilm growth (Fig. 2a-b). Strong advective transport at high *Pe* conditions prevents extensive substrate consumption near the inlet, with short fluid residence times promoting the substrate delivery to downstream locations (compare substrate concentration fields at P2 and P3 in Fig. 2b). As a consequence, biofilms of simulation BF51 experience higher average substrate concentrations ($< C_{bf} > = \int C \, dV_B \, / \, V_B$; Fig. 2d) and grow more uniformly across the domain than BF21. High *Pe* also causes the highest $< R_c >$ to occur at lower ϕ (compare brown (BF51) and green (BF21) symbols in Fig. 2c) and thus, results in the simulated ϕ-κ curves to be closer to KC (Fig. 2a). In contrast, fast reaction compared to diffusion (i.e., high *Da* conditions) fosters fast localized biofilm growth and substrate consumption (compare blue (BF25) and green (BF21) symbols in Fig. 2c). Because most substrate (95%) is consumed by the biofilms on the left-most solid for BF25 (P4), biofilm growth occurs primarily very close to the inlet and biofilms further downstream are substrate limited (Fig. 2b). Therefore, biofilms grow predominantly near the inlet leading to a more rapid reduction in κ for a given reduction in ϕ for BF25 than BF21.

3.2 Threshold Porosity and Pore Geometry

To investigate the evolution of porosity and permeability as a function of flow (*Pe*) and reaction (*Da*) conditions, we identified the threshold porosity (ϕ_{thrd}) at which the growing biofilm leads to a substantial deviation from the KC equation (Fig. 3a). This is the point where the development of a steep concentration gradient within the simulation domain leads to non-homogeneous biofilm growth. As a consequence, the initial REV assumption no longer holds. ϕ_{thrd} were determined as the maximum porosity at which

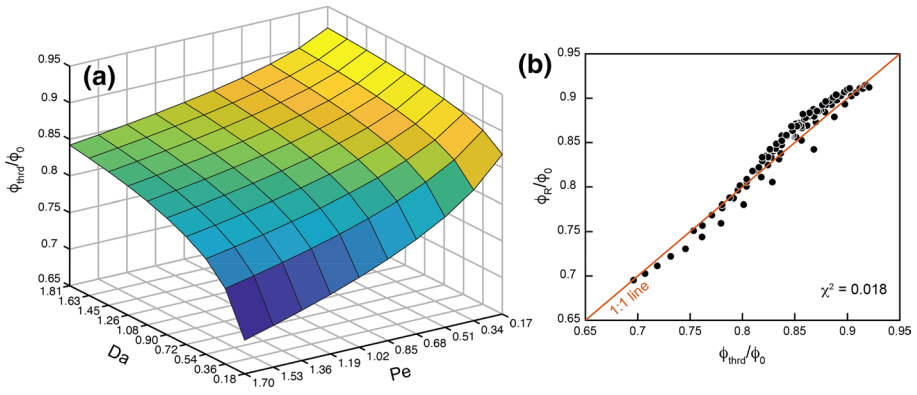

Fig. 3 (**a**) The threshold porosity (ϕ_{thrd}) where ϕ-κ curves start to deviate from KC at $\varepsilon = 10^{-4}$. The mesh points are *Pe* and *Da* of each simulation run for BFs. (**b**) The scatter plot comparing ϕ_{thrd} and the simulated porosity at the maximum volume-averaged reaction rate $< R_c > (\phi_R)$. χ^2 denotes the goodness of fit

$(\kappa/\kappa_0)_{model}$-$(\kappa/\kappa_0)_{KC}$ exceeds a threshold $\varepsilon = 10^{-4}$. The results underline that the effect of biofilm growth on flow emerges at high porosities at slow flow (i.e., low *Pe*) and fast reaction conditions (i.e., high *Da*) but occur only at low porosity under slow reaction (i.e.,. low *Da*) and fast advection conditions (i.e., high *Pe*).

The estimated ϕ_{thrd} were also compared with porosities at the maximum volumetric rate $< R_c >$ (ϕ_R; Fig. 3b). ϕ_{thrd} determined with different ε (10^{-3}, 10^{-4}, and 10^{-5}) shows that the relationship between ϕ_{thrd} and ϕ_R is not sensitive to ε (Figure S2). Figure 3b shows clear positive correlations with the slope of 1 indicating the correspondence between ϕ_{thrd} and the porosity at the maximum reaction rate. This correspondence suggests that knowing ϕ_{thrd} can be particularly useful in optimizing the efficiency of bioengineering applications because the time when permeability and reaction rates start to decrease can be approximated a priori.

We further extended the analysis to assess the effect of pore geometry on the evolution of porosity and permeability. For this purpose, we derived functional approximations from the simulation results of BFs (Equations S1 and S2) and applied them to simulation results with different pore geometries, GMs (Table 1). When tortuosity was increased by changing only the grain distribution (GM1-2), the simulation results show slightly higher κ than BF45, but the difference is largely negligible (Fig. 4). This similarity may not be surprising because flow and reaction properties were maintained under the same *Pe* and *Da* condition despite the changes in pore geometry. However, ϕ-κ curves of GM3-4 are also similar to BF45 despite different *Pe* and *Da* (Table 1). Here, the difference in *Pe* and *Da* between BF45 and GM3-4 solely originates from different grain sizes, hence initial porosities. To account for the effect of different porosities on *Pe* and *Da*, we introduced the scaling factor F ($=l_l/l_\phi$) relating pore throat sizes of porous media with different initial porosities with a solid circular grain ($l_\phi = 0.5L_y\text{-}L_y\sqrt{(1-\phi)/\pi}$) to the pore throat size of BFs (l_1), on which the curve fitting analysis is originally based (see Supplementary Information). The scaled fitting curves (Equations S1 and S2) correctly capture the evolution of not only GM3-4 but also GM5-6 (different l but the same ϕ_0; Table 1) which illustrate the earlier onset and more rapid reduction in κ than BF45 (Fig. 4). These results indicate that the effect of biofilm growth on porosity and permeability can be captured when accounting for *Pe*, *Da,* and initial porosity (and hence F) conditions for idealized porous media consisting of circular grains with well-defined characteristic lengths.

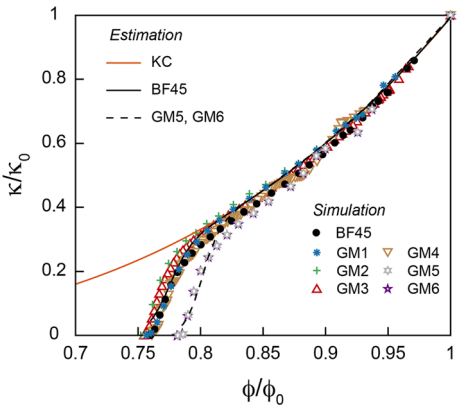

Fig. 4 ϕ-κ curves of six simulations with a set of idealized pore geometries (GM1 – GM6) compared to the reference case (BF45), where $Pe = 0.85$ and $Da = 0.90$. Detailed simulation conditions can be found in Table 1

3.3 Permeable Biofilms

Porous media with uniform permeable biofilms (HPBs* and LPBs*) exhibit, unsurprisingly, higher bulk permeabilities than impermeable biofilms (NBFs*; Fig. 5a). Advective flows are maintained even when the pore throats are completely clogged, reflected in finite permeabilities for HPB17 and LPB17 at ϕ_c (Fig. 5a). A notable difference between permeable and impermeable biofilm simulations is the slopes of ϕ-κ curves. Permeabilities of uniformly distributed, non-porous low and highly permeable biofilms (LPBs* and HPBs*) decrease continuously until intermediate ϕ/ϕ_0 and increase again at low ϕ/ϕ_0, while the slope for non-porous impermeable biofilms (NBFs*) decreases continuously with ϕ/ϕ_0. At $\phi/\phi_0 = 0.64$ (LPB10 and HPB10), maximum flow velocities for both HPB10 and LPB10 occur in the pore water (Fig. 5b), but a much larger fraction of flow occurs through the free fluid for LPB10 than HPB10 (85.6% and 70% of total fluid flux, respectively). The velocity profiles at the critical porosity $\phi_c = 0.21$ ($\phi_c/\phi_0 = 0.33$), where the pore throat at $nx = 100$ is completely clogged (LPB17 and HBP17), show lower maximum flow velocities than LPB10 and HBP10 that occur near the center of the biofilm with a more pronounced focusing of flow into the low permeability biofilm (LPB17), reflecting stronger contrast of flow velocities in biofilm and pore grid cells (Fig. 5b).

Velocity profiles depending on biofilm permeability indicate that varying shear stresses are imposed on pore–biofilm interfaces. For example, the shear stress ($\nu_f \rho |\partial u_x|/|\partial y|$) at a pore–biofilm interface for LPB10 is about seven times larger than that for HPB10 at the same location. If shear-induced sloughing was an important biofilm detachment mechanism (Knutson et al. 2005; Paul et al. 2012), strong stress imposed on biofilms with low permeability would prevent large biofilm accumulation promoting more uniform spatial biofilm distribution (Pintelon et al. 2012).

The simulated ϕ-κ curves for permeable biofilms (PBs) share a few similar responses to *Pe* and *Da* with impermeable ones (BFs; Fig. 6a). This includes relatively uniform biofilm growth under high *Pe* (PB3 and PB4) and preferential growths of upstream biofilm under high *Da* (PB5 and PB6) (Fig. 6b). The average solute concentrations in biofilms ($< C_{bf} >$) and average substrate consumption rates ($< R_c >$) of PBs also show largely similar responses to *Pe* and *Da* compared to BFs (Fig. 6c-d). However, PBs experience higher $< C_{bf} >$ and $< R_c >$ than BFs at the same *Pe* and *Da*. This is because

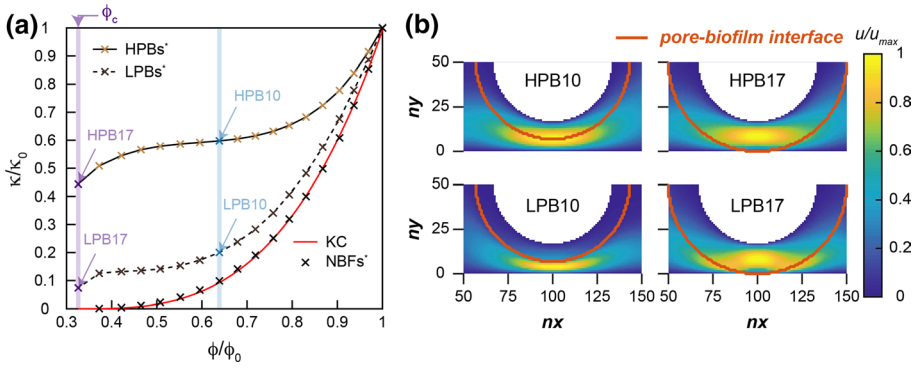

Fig. 5 (**a**) ϕ-κ curves of uniformly growing permeable biofilms with high (HPBs*) and low permeabilities (LPBs*), and impermeable biofilms (NBFs*). Two biofilm thicknesses ($0.1L_y$ and $0.17L_y$) were selected to investigate (**b**) the velocity profiles across a pore throat

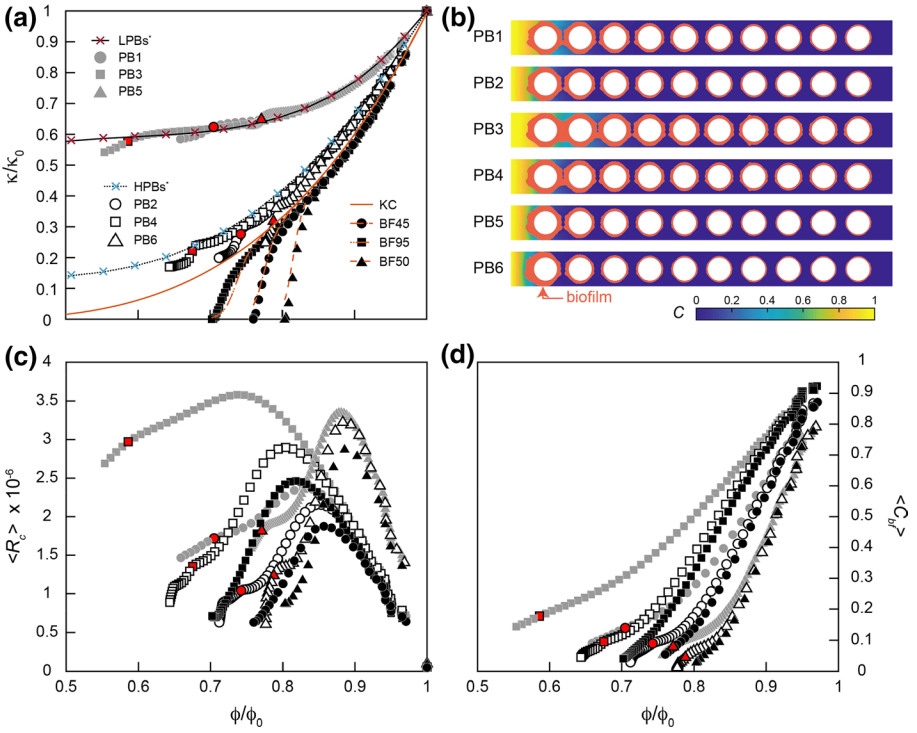

Fig. 6 (**a**) Simulated ϕ-κ curves for permeable biofilms (PB1 – PB6) and three impermeable biofilms (BF5, BF41, and BF45) where PBs and BFs with matching *Pe* and *Da* conditions are marked with the same symbol. HPBs*, LPBs*, KC are simulations with static, uniform biofilms with high, low, and no biofilm permeability, respectively. Red-filled markers indicate when the most upstream pore throat is first clogged by biofilms. (**b**) Spatial biofilms and substrate distributions at the time indicated by the red-filled markers of PBs. (**c**) Volume-averaged substrate consumption rate ($<R_c>$) and (**d**) volume-averaged concentration distribution within biofilm grid cells ($<C_{bf}>$)

of the facilitated downstream solute transport which also leads to maximum $<R_c>$ to occur at lower ϕ than BFs by delaying the onset of non-uniform biofilm growth.

ϕ-κ curves from simulations with spatially varying biofilms (PBs) differ from those with uniform biofilm distributions (HPBs* and LPBs* in Fig. 6). Unlike BFs, however, the rapid reduction in κ occurs primarily after the clogging of the pore throat nearest to the inlet (red-filled markers in Fig. 6) for PBs. Moreover, the rapid reduction in κ slowed down after clogging occurred because further biofilm growth does not significantly influence the flow velocity through the pore throat. As a result, the reduction in κ is much less for PBs than BFs, especially for high permeable biofilms (PB1, PB3, and PB5). This result shows that biofilm permeability is an essential factor determining the sensitivity of porosity–permeability relations to *Pe* and *Da* conditions.

3.4 Biofilm Cell Density

The effect of biofilm packing was considered by adjusting the maximum biomass density B_{max} based on the biofilm porosity ($B_{max,\mathrm{BPs}}=(1-\phi_{BPs})\times B_{max,\mathrm{BF45}}$). To reflect the unique nature of fluid in biofilm structures (Flemming and Wingender 2010; Schmitt and Flemming 1999), biofilm porosity is not accounted for in calculating total porosity. This implies that the water in the biofilm is not or negligibly contributing to the effective porosity, in line with previous studies (e.g., Cunningham et al. 1991). As a result, ϕ-κ curves with imposed uniform biofilm distributions but with different biofilm porosities—NBPs*, HBPs*, LBPs* (Fig. 7a)—exhibit patterns identical to non-porous permeable uniform biofilm cases—NBFs*, HPBs*, LPBs* (Fig. 5a)—respectively.

The effect of maximum biofilm cell density is visible in dynamic biofilm growth simulations (BP1-3). The results show rapid growth of biofilm volume without substantial increase in substrate consumption because of the reduced B_{max} and Da (Eq. 6). For example, B_{max} and Da of BP1 is 10% of the reference case BF45 (Table 1). Higher biofilm porosity (i.e., lower B_{max}) results in relatively homogeneous substrate distribution promoting

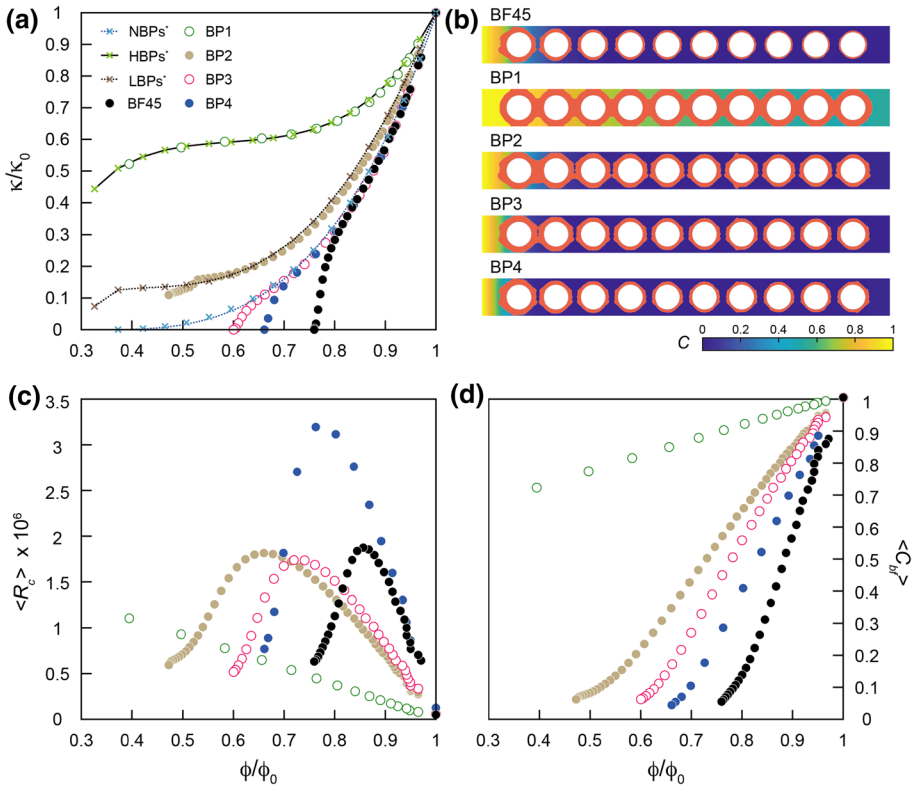

Fig. 7 (**a**) Simulated ϕ-κ curves with biofilm porosity (BP1 – BP4), and a non-porous impermeable biofilm case (BF45). HBPs*, LBPs*, and NBPs* are uniformly distributed biofilms with biofilm porosity of 0.9, 0.63, and 0.56, respectively. (**b**) Spatial biofilms and substrate distributions at the simulations showing complete pore closure for the first time, (**c**) volume-averaged substrate consumption rate ($<R_c>$), and (**d**) volume-averaged concentration within biofilm grid cells ($<C_{\mathrm{bf}}>$) of BPs and BF45

more uniform biofilm growth, which also can be understood as a consequence of the low *Da* (Fig. 7a-b and Table 1). Thus, the simulation with the highest biofilm porosity and the lowest *Da*, BP1, shows more uniform substrate and biofilm distributions than those with lower biofilm porosities and higher *Da*, BP2-3. As a result of uniform biofilm growth across the domain, BP1 follows the ϕ-κ curve of HBPs*, while BP2-3 deviate from the corresponding uniform distribution curves (LBPs* and NBPs*; Fig. 7a). The uniform biofilm growth of BP1 is also identifiable from $<R_c>$, which keeps increasing with decreasing porosity until complete pore closure (Fig. 7c). At later times, unlike BP1, BP2-3 show a decrease in $<R_c>$ due to non-uniform biofilm growth.

Although the reaction conditions (Da/B_{max}) of BP1-3 were maintained the same as for BF45, these cases illustrate various evolution patterns of $<R_c>$. At early times where $<R_c>$ increases with decreasing ϕ/ϕ_0, simulation cases with lower biofilm porosity exhibit higher $<R_c>$ at a given porosity (Fig. 7c). For example, at $\phi/\phi_0 = 0.9$, the sequence of $<R_c>$ is BF45 ($\phi_{BP} = 0$) > BP3 ($\phi_{BP} = 0.56$) > BP2 ($\phi_{BP} = 0.63$) > BP1 ($\phi_{BP} = 0.9$). Here, ϕ_{BP} does not affect total medium porosity (ϕ); thus, the volume of biofilm is identical for BP1-3 and BF45 at a fixed porosity condition. The difference in $<R_c>$ stems from different biofilm porosity conditions where, for example, a high biofilm porosity results in a low biomass and hence, low $<R_c>$. As expected, when *Da* is increased by increasing the rate constant *k* (compare BP4 to BP3), biofilm growth of porous biofilms becomes less uniform showing early deviation from the ϕ-κ curve of KC (Fig. 7a-b), higher $<R_c>$ and rapid reduction of $<R_c>$ after reaching the maximum $<R_c>$ (Fig. 7c), and lower $<C_{bf}>$ due to fast substrate consumption (Fig. 7d). This result shows that biofilm porosity substantially alters the co-evolution of porosity and permeability, altering the porosity at which reaction rates are maximal, and promoting uniform biofilm growth by reducing *Da*.

4 Conclusions

This study investigated pore-scale factors that determine the evolution of porosity and permeability driven by biofilm growth. Our two-dimensional pore-scale reactive transport simulations demonstrate that pore-scale heterogeneity, hydrological features, and biofilm characteristics are important factors shaping the evolution of porosity and permeability. Localized biomass growth gives rise to the differentiation of REVs for porosity and permeability. Bioclogging, manifested in a strong reduction in permeability associated with a small reduction in porosity, depends on flow and reaction conditions, reflected by *Pe* and *Da* numbers. Fast consumption of growth-limiting nutrient at high *Da* conditions intensifies preferential biofilm growth and results in the deviation from KC with rapid permeability reduction. In contrast, fast advection under high *Pe* conditions homogenizes the concentration distribution along the main flow path and hence, promotes uniform biofilm growth weakening the rapid permeability reduction. The *Pe* and *Da* analysis also revealed that maximum substrate consumption rates, which is determined by the balance between substance delivery (i.e., permeability) and biomass abundance (i.e., biomass density), occur when permeability begins to deviate from commonly observed permeability–porosity relationships such as, for example, the Kozeny–Carman equation (Schultz et al. 2019; Zhang et al. 2000).

Estimating the permeability of a porous medium from porosities in the presence of biofilm growth also depends on the characteristics of the pore geometry and biofilm. The effect of geometric factors, including tortuosity and pore throat sizes, on the evolution of

porous media can be explained—at least in the idealized porous media considered here—in terms of *Pe* and *Da* as well with a scaling factor *F* accounting for pore throat sizes set by different initial porosities. When biofilm porosity and permeability are considered, ϕ-κ curves are substantially different from non-porous impermeable biofilm simulations. When biofilms are non-porous, permeable, porous media exhibit higher bulk permeability at a given porosity and permeabilities become less sensitive to non-uniform biofilm growth depending on *Pe* and *Da*. Biofilm porosity promotes uniform biofilm growth as a reduced biomass density at a given porosity allows for downstream transport of growth-limiting nutrients. While capturing important patterns, we note that in natural subsurface environments, heterogeneities in a three-dimensional porous medium structure may also substantially influence the evolution of porosity and permeability (Carrel et al. 2018; Thullner 2010) under microbial growth, with patchy biofilms (Deschesne et al. 2007; Nunan et al. 2002) leading to bioclogging. Microbial growth and distribution can also be affected actively (chemotaxis, quorum sensing) or passively (e.g., shear-stress-induced sloughing) (Ford and Harvey 2007; Kim and Fogler 2000; Solano et al. 2014), highlighting the importance of detailed experimental studies.

Supplementary Information The online version contains supplementary material available at https://doi.org/10.1007/s11242-021-01654-7.

Acknowledgements We thank two anonymous reviewers for thoughtful comments that helped to significantly improve the manuscript. This work was supported by the U.S. Department of Energy, Office of Science, Office of Biological and Environmental Research, Genomic Science Program under Award Number DE-SC0020373, and the Institute for Korea Spent Nuclear Fuel (iKSNF) and National Research Foundation of Korea (NRF) grant funded by Ministry of Science and ICT (MSIT) under Award Number 2021M2E1A1085202. This study was also supported in part by resources and technical expertise from the Georgia Advanced Computing Resource Center, a partnership between the University of Georgia's Office of the Vice President for Research and Office of the Vice President for Information Technology. We have no conflict of interest to declare. The LB code is available at BitBucket: https://bitbucket.org/MeileLab/jung_biofgrowth

References

Abdel Aal, G.Z., Atekwana, E.A., Atekwana, E.A.: Effect of bioclogging in porous media on complex conductivity signatures. J. Geophys. Res. (2010). https://doi.org/10.1029/2009JG001159

Battiato, I., Tartakovsky, D.M., Tartakovsky a. M Scheibe T: On breakdown of macroscopic models of mixing-controlled heterogeneous reactions in porous media. Adv. Water Resour. **32**, 1664–1673 (2009). https://doi.org/10.1016/j.advwatres.2009.08.008

Baveye, P., Vandevivere, P., Hoyle, B.L., DeLeo, P.C., de Lozada, D.S.: Environmental impact and mechanisms of the biological Clogging of saturated soils and aquifer materials. Crit. Rev. Environ. Sci. Technol. **28**, 123–191 (1998). https://doi.org/10.1080/10643389891254197

Benioug, M., Golfier, F., Oltéan, C., Buès, M.A., Bahar, T., Cuny, J.: An immersed boundary-lattice Boltzmann model for biofilm growth in porous media. Adv. Water Resour. **107**, 65–82 (2017). https://doi.org/10.1016/j.advwatres.2017.06.009

Bhatnagar, P.L., Gross, E.P., Krook, M.: A model for collision processes in gases. I. Small amplitude processes in charged and neutral one-component systems. Phys. Rev. **94**, 511–525 (1954). https://doi.org/10.1103/PhysRev.94.511

Carrel, M., Morales, V.L., Dentz, M., Derlon, N., Morgenroth, E., Holzner, M.: Pore-scale hydrodynamics in a progressively bioclogged three-dimensional porous medium: 3-D particle tracking experiments and stochastic transport modeling. Water Resour. Res. (2018). https://doi.org/10.1002/2017WR021726

Cunningham, A.B., Characklls, W.G., Abedeen, F., Crawford, D.: Influence of biofilm accumulation on porous media hydrodynamics. Environ. Sci. Technol. **25**, 1305–1311 (1991). https://doi.org/10.1021/es00019a013

Davarzani, H., Marcoux, M., Quintard, M.: Theoretical predictions of the effective thermodiffusion coefficients in porous media. Int. J. Heat Mass Transf. **53**, 1514–1528 (2010). https://doi.org/10.1016/j.ijheatmasstransfer.2009.11.044

Deschesne, A., Pallud, C., Grundmann, G.L.: Spatial distribution of bacteria at the microscale in soil. Spat. Distrib. Microbes Environ. (2007). https://doi.org/10.1007/978-1-4020-6216-2_4

Doyen, P.M.: Permeability, conductivity, and pore geometry of sandstone. J. Geophys. Res. **93**, 7729 (1988). https://doi.org/10.1029/JB093iB07p07729

Ellis, D.E., Lutz, E.J., Odom, J.M., Buchanan, R.J., Bartlett, C.L., Lee, M.D., Harkness, M.R., DeWeerd, K.A.: Bioaugmentation for accelerated In Situ anaerobic bioremediation. Environ. Sci. Technol. **34**, 2254–2260 (2000). https://doi.org/10.1021/es990638e

Ezeuko, C.C., Sen, A., Grigoryan, A., Gates, I.D.: Pore-network modeling of biofilm evolution in porous media. Biotechnol. Bioeng. **108**, 2413–2423 (2011). https://doi.org/10.1002/bit.23183

Flemming, H.C., Wingender, J.: The biofilm matrix. Nat. Rev. Microbiol. **8**, 623–633 (2010). https://doi.org/10.1038/nrmicro2415

Ford, R.M., Harvey, R.W.: Role of chemotaxis in the transport of bacteria through saturated porous media. Adv. Water Resour. **30**, 1608–1617 (2007). https://doi.org/10.1016/j.advwatres.2006.05.019

Ginzbourg, I., Adler, P.M.: Boundary flow condition analysis for the three-dimensional lattice boltzmann model. J. Phys. **II**(4), 191–214 (1994)

Golfier, F., Zarcone, C., Bazin, B., Lenormand, R., Lasseux, D., Quintard, M.: On the ability of a darcy-scale model to capture wormhole formation during the dissolution of a porous medium. J. Fluid Mech. **457**, 213–254 (2002). https://doi.org/10.1017/S0022112002007735

Halan, B., Buehler, K., Schmid, A.: Biofilms as living catalysts in continuous chemical syntheses. Trends Biotechnol. **30**, 453–465 (2012). https://doi.org/10.1016/j.tibtech.2012.05.003

Han, L., Liu, P., Peng, Y., Lin, J., Wang, Q., Ma, Y.: Engineering the biosynthesis of novel rhamnolipids in escherichia coli for enhanced oil recovery. J. Appl. Microbiol. **117**, 139–150 (2014). https://doi.org/10.1111/jam.12515

Heße, F., Radu, F.A., Thullner, M., Attinger, S.: Upscaling of the advection-diffusion-reaction equation with Monod reaction. Adv. Water Resour. **32**, 1336–1351 (2009). https://doi.org/10.1016/j.advwatres.2009.05.009

Hommel, J., Coltman, E., Class, H.: Porosity-permeability relations for evolving pore space: a review with a focus on (Bio-)geochemically altered porous media. Transp. Porous Media. **124**, 589–629 (2018). https://doi.org/10.1007/s11242-018-1086-2

Hosseininoosheri, P., Lashgari, H.R., Sepehrnoori, K.: A novel method to model and characterize in-situ bio-surfactant production in microbial enhanced oil recovery. Fuel **183**, 501–511 (2016). https://doi.org/10.1016/j.fuel.2016.06.035

Huber, C., Shafei, B., Parmigiani, A.: A new pore-scale model for linear and non-linear heterogeneous dissolution and precipitation. Geochim. Cosmochim. Acta. **124**, 109–130 (2014). https://doi.org/10.1016/j.gca.2013.09.003

Jung, H., Meile, C.: Upscaling of microbially driven first-order reactions in heterogeneous porous media. J. Contam. Hydrol. **224**, 103483 (2019). https://doi.org/10.1016/j.jconhyd.2019.04.006

Jung, H., Meile, C.: Mathematical investigation of microbial quorum sensing under various flow conditions. PeerJ **8**, e9942 (2020). https://doi.org/10.7717/peerj.9942

Kang, Q., Zhang, D., Chen, S.: Simulation of dissolution and precipitation in porous media. J. Geophys. Res. Solid Earth. **108**, 1–10 (2003). https://doi.org/10.1029/2003JB002504

Kao, C.M., Chen, S.C., Liu, J.K.: Development of a biobarrier for the remediation of PCE-contaminated aquifer. Chemosphere **43**, 1071–1078 (2001). https://doi.org/10.1016/S0045-6535(00)00190-9

Kim, D.-S., Fogler, H.S.: Biomass evolution in porous media and its effects on permeability under starvation conditions. Biotechnol. Bioeng. **69**, 47–56 (2000). https://doi.org/10.1002/(SICI)1097-0290(20000705)69:1%3c47::AID-BIT6%3e3.0.CO;2-N

Knutson, C.E., Werth, C.J., Valocchi, A.J.: Pore-scale simulation of biomass growth along the transverse mixing zone of a model two-dimensional porous medium. Water Resour. Res. **41**, 1–12 (2005). https://doi.org/10.1029/2004WR003459

Komlos, J., Cunningham, A.B., Kamper, A.K., Sharp, R.R.: Biofilm barriers to contain and degrade dissolved trichloroethylene. Environ. Prog. **23**, 69–77 (2004). https://doi.org/10.1002/ep.10003

Krüger, T., Kusumaatmaja, H., Kuzmin, A., Shardt, O., Silva, G., Viggen, E.M.: The Lattice Boltzmann Method. Springer International Publishing, Cham (2017)

Latt, J., Malaspinas, O., Kontaxakis, D., Parmigiani, A., Lagrava, D., Brogi, F., Belgacem, M.B., Thorimbert, Y., Leclaire, S., Li, S., Marson, F., Lemus, J., Kotsalos, C., Conradin, R., Coreixas, C., Petkantchin, R., Raynaud, F., Beny, J., Chopard, B.: Palabos: parallel lattice boltzmann solver. Comput. Math. with Appl. **81**, 334–350 (2021). https://doi.org/10.1016/j.camwa.2020.03.022

Lazar, I., Petrisor, I.G., Yen, T.F.: Microbial enhanced oil recovery (MEOR). Pet. Sci. Technol. **25**, 1353–1366 (2007). https://doi.org/10.1080/10916460701287714

Lendvay, J.M., Löffler, F.E., Dollhopf, M., Aiello, M.R., Daniels, G., Fathepure, B.Z., Gebhard, M., Heine, R., Helton, R., Shi, J., Krajmalnik-Brown, R., Major, C.L., Barcelona, M.J., Petrovskis, E., Hickey, R., Tiedje, J.M., Adriaens, P.: Bioreactive barriers: a comparison of bioaugmentation and biostimulation for chlorinated solvent remediation. Environ. Sci. Technol. **37**, 1422–1431 (2003). https://doi.org/10.1021/es025985u

Luquot, L., Gouze, P.: Experimental determination of porosity and permeability changes induced by injection of CO2 into carbonate rocks. Chem. Geol. **265**, 148–159 (2009). https://doi.org/10.1016/j.chemgeo.2009.03.028

MacQuarrie, K.T.B., Sudicky, E.A.: Multicomponent simulation of wastewater-derived nitrogen and carbon in shallow unconfined aquifers. J. Contam. Hydrol. **47**, 53–84 (2001). https://doi.org/10.1016/S0169-7722(00)00137-6

Miranda, A.F., Ramkumar, N., Andriotis, C., Höltkemeier, T., Yasmin, A., Rochfort, S., Wlodkowic, D., Morrison, P., Roddick, F., Spangenberg, G., Lal, B., Subudhi, S., Mouradov, A.: Applications of microalgal biofilms for wastewater treatment and bioenergy production. Biotechnol. Biofuels. **10**, 120 (2017). https://doi.org/10.1186/s13068-017-0798-9

Mostaghimi, P., Blunt, M.J., Bijeljic, B.: Computations of absolute permeability on micro-CT images. Math. Geosci. **45**, 103–125 (2013). https://doi.org/10.1007/s11004-012-9431-4

Nunan, N., Wu, K., Young, I.M., Crawford, J.W., Ritz, K.: In situ spatial patterns of soil bacterial populations, mapped at multiple scales, in an arable soil. Microb. Ecol. **44**, 296–305 (2002). https://doi.org/10.1007/s00248-002-2021-0

Paul, E., Ochoa, J.C., Pechaud, Y., Liu, Y., Liné, A.: Effect of shear stress and growth conditions on detachment and physical properties of biofilms. Water Res. **46**, 5499–5508 (2012). https://doi.org/10.1016/j.watres.2012.07.029

Peszynska, M., Trykozko, A., Iltis, G., Schlueter, S., Wildenschild, D.: Biofilm growth in porous media: experiments, computational modeling at the porescale, and upscaling. Adv. Water Resour. **95**, 288–301 (2016). https://doi.org/10.1016/j.advwatres.2015.07.008

Picioreanu, C., van Loosdrecht, M.C.M., Heijnen, J.J.: Mathematical modeling of biofilm structure with a hybrid differential-discrete cellular automaton approach. Biotechnol. Bioeng. **58**, 101–116 (1998). https://doi.org/10.1002/(SICI)1097-0290(19980405)58:1%3c101::AID-BIT11%3e3.0.CO;2-M

Pintelon, T.R.R., Graf von der Schulenburg, D.A., Johns, M.L.: Towards optimum permeability reduction in porous media using biofilm growth simulations. Biotechnol. Bioeng. **103**, 767–779 (2009). https://doi.org/10.1002/bit.22303

Pintelon, T.R.R., Picioreanu, C., van Loosdrecht, M.C.M., Johns, M.L.: The effect of biofilm permeability on bio-clogging of porous media. Biotechnol. Bioeng. **109**, 1031–1042 (2012). https://doi.org/10.1002/bit.24381

Quintard, M., Whitaker, S.: Transport in ordered and disordered porous media III: closure and comparison between theory and experiment. Transp. Porous Media. **15**, 31–49 (1994). https://doi.org/10.1007/BF01046157

Rittmann, B., McCarty, P.: Environmental Biotechnology: Principles and Applications. McGraw-Hill, New York (2001). https://www.accessengineeringlibrary.com/content/book/9781260440591

Rooney, L.M., Amos, W.B., Hoskisson, P.A., McConnell, G.: Intra-colony channels in *E coli* function as a nutrient uptake system. ISME J (2020). https://doi.org/10.1038/s41396-020-0700-9

Schmitt, J., Flemming, H.-C.: Water binding in biofilms. Water Sci. Technol. (1999). https://doi.org/10.1016/S0273-1223(99)00153-5

Schulz, R., Ray, N., Zech, S., Rupp, A., Knabner, P.: Beyond kozeny–carman: predicting the permeability in porous media. Transp. Porous Media. **130**, 487–512 (2019). https://doi.org/10.1007/s11242-019-01321-y

Solano, C., Echeverz, M., Lasa, I.: Biofilm dispersion and quorum sensing. Curr. Opin. Microbiol. **18**, 96–104 (2014). https://doi.org/10.1016/j.mib.2014.02.008

Soulaine, C., Roman, S., Kovscek, A., Tchelepi, H.A.: Mineral dissolution and wormholing from a pore-scale perspective. J. Fluid Mech. **827**, 457–483 (2017). https://doi.org/10.1017/jfm.2017.499

Stolpovsky, K., Gharasoo, M., Thullner, M.: The impact of pore-size heterogeneities on the spatiotemporal variation of microbial metabolic activity in porous media. Soil Sci. **177**, 98–110 (2012). https://doi.org/10.1097/SS.0b013e318241105d

Stoodley, P., Sauer, K., Davies, D.G., Costerton, J.W.: Biofilms as complex differentiated communities. Annu. Rev. Microbiol. **56**, 187–209 (2002). https://doi.org/10.1146/annurev.micro.56.012302.160705

Tang, Y., Valocchi, A.J., Werth, C.J., Liu, H.: An improved pore-scale biofilm model and comparison with a microfluidic flow cell experiment. Water Resour. Res. **49**, 8370–8382 (2013). https://doi.org/10.1002/2013WR013843

Thullner, M.: Comparison of bioclogging effects in saturated porous media within one- and two-dimensional flow systems. Ecol. Eng. **36**(2), 176196 (2010). https://doi.org/10.1016/j.ecoleng.2008.12.037

Thullner, M., Baveye, P.: Computational pore network modeling of the influence of biofilm permeability on bioclogging in porous media. Biotechnol. Bioeng. **99**, 1337–1351 (2008). https://doi.org/10.1002/bit.21708

Vandevivere, P.: Bacterial clogging of porous media: a new modelling approach. Biofouling **8**(4), 281291 (1995). https://doi.org/10.1080/0892701950937828

Wilking, J.N., Zaburdaev, V., De Volder, M., Losick, R., Brenner, M.P., Weitz, D.A.: Liquid transport facilitated by channels in bacillus subtilis biofilms. Proc. Natl. Acad. Sci. **110**, 848–852 (2013). https://doi.org/10.1073/pnas.1216376110

Wood, B.D.: The role of scaling laws in upscaling. Adv. Water Resour. **32**, 723–736 (2009). https://doi.org/10.1016/j.advwatres.2008.08.015

Xie, M., Mayer, K.U., Claret, F., Alt-Epping, P., Jacques, D., Steefel, C., Chiaberge, C., Simunek, J.: Implementation and evaluation of permeability-porosity and tortuosity-porosity relationships linked to mineral dissolution-precipitation. Comput. Geosci. **19**, 655–671 (2015). https://doi.org/10.1007/s10596-014-9458-3

Zhang, T.C., Bishop, P.L.: Density, porosity, and pore structure of biofilms. Water Res. **28**, 2267–2277 (1994). https://doi.org/10.1016/0043-1354(94)90042-6

Zhang, D., Zhang, R., Chen, S., Soll, W.E.: Pore scale study of flow in porous media: Scale dependency, REV, and statistical REV. Geophys. Res. Lett. **27**, 1195–1198 (2000). https://doi.org/10.1029/1999GL011101